Unraveling the Sinuous Grain Boundaries in Graphene

Zhuhua Zhang, Yang Yang, Fangbo Xu, Luqing Wang, and Boris I. Yakobson*

Grain boundaries (GBs) in graphene are stable strings of pentagon-heptagon dislocations. The GBs have been believed to favor an alignment of dislocations, but increasing number of experiments reveal diversely sinuous GB structures whose origins have long been elusive. Based on dislocation theory and first-principles calculations, an extensive analysis of the graphene GBs is conducted and it is revealed that the sinuous GB structures, albeit being longer than the straight forms, can be energetically optimal once the global GB line cannot bisect the tilt angle. The unusually favorable sinuous GBs can actually decompose into a series of well-defined bisector segments that effectively relieve the in-plane stress of edge dislocations, and the established atomic structures closely resemble recent experimental images of typical GBs. In contrast to previously used models, the sinuous GBs show improved mechanical properties and are distinguished by a sizable electronic transport gap, which may open potential applications of polycrystalline graphene in functional devices.

1. Introduction

Recently, graphene research has experienced limitations, caused by a number of issues, in delivering its potential into applications.[1,2] In particular, graphene is prone to a rich variety of defects during fabrication by means of different techniques,[3–6] resulting in severely degraded performance as measured. The most common technique—the chemical vapor deposition (CVD) method—unavoidably produces polycrystalline graphene samples.[7–12] During the course of CVD growth, graphene domains are nucleated randomly on substrates; if the domains are misoriented with each other, their growth and coalescence result in formation of grain boundaries (GBs).[13,14] As topological linear defects, GBs are extremely stable and could create long-range stress fields in the two-dimensional crystal.[15,16] Not only is the landscape of graphene strongly modified,[17] but also its mechanical,[16,18–20] electrical[21–29] and optical properties[29] are significantly impaired by the GBs. Thus it is imperative

to fully understand the GBs in terms of structures and properties. While the GBs in graphene have been confirmed to be strings of pear-shaped pentagon-heptagon (5|7) edge dislocations,[30,31] the flexible organization of dislocations gives rise to diverse GB shapes, e.g., straight lines, loops[32] and sinuous shapes. Energetically, identical edge dislocations should favor a vertical alignment,[17] and the formed GB will bisect the tilt angle of the misoriented grains. The energetically favored bisector GBs are indeed observed in highly oriented pyrolytic graphite as linear periodic superstructures,[33–35] in line with recent theoretical models.[17,31,36] However, the situation becomes quite different in CVD-grown graphene, wherein the grain sizes become much smaller than those in exfoliated samples and the GB shapes turn into sinuous.[7–11] Atomic scale characterizations revealed that the sinuous GBs usually do not bisect the misorientation (tilt) angle of domains over a nanometer length,[8,10] thus belonging to asymmetric (or nonbisector) type. Considering the abundance of asymmetric GBs in CVD-grown samples, determining their structures and their influence on electronic behavior is hence particularly important for designing graphene devices with desired performance. Despite extensive theoretical effort on the nonbisector GBs,[19–21,37,38] little is know about their preferred structures and even less about the modification of properties that they cause. What is more, no physical rule is proposed for elucidating the formation mechanism of sinuous grain boundaries prevalent in experimental observations.

Here, we perform an analytical study of asymmetric GBs in graphene and reveal a universal rule for reaching their ground state structures. In contrast to the commonly used linear models, we find that the nonbisector GBs are preferably composed of slant bisector segments that form a sinuous shape, which closely resembles recent experimental images. The orientation, geometry and atomic structures of the bisector segments in the sinuous grain boundaries (s-GBs) can be well quantified by the domains' matching vectors and are verified by extensive atomistic calculations. Further, the s-GBs are distinct in showing enhanced mechanical strength and semiconducting transport behavior. These findings not only serve as a general guidance for understanding the morphology of GBs in two-dimensional atomic crystals but also offer a new insight into their structure-property relationships.

Dr. Z. Zhang, Y. Yang, F. Xu, L. Wang,
Prof. B. I. Yakobson
Department of Materials Science and Nanoengineering
Department of Chemistry, and the Smalley Institute
for Nanoscale Science and Technology
Rice University
Houston, TX 77005, United States
E-mail: biy@rice.edu

ADVANCED
FUNCTIONAL
MATERIALS
www.afm-journal.de
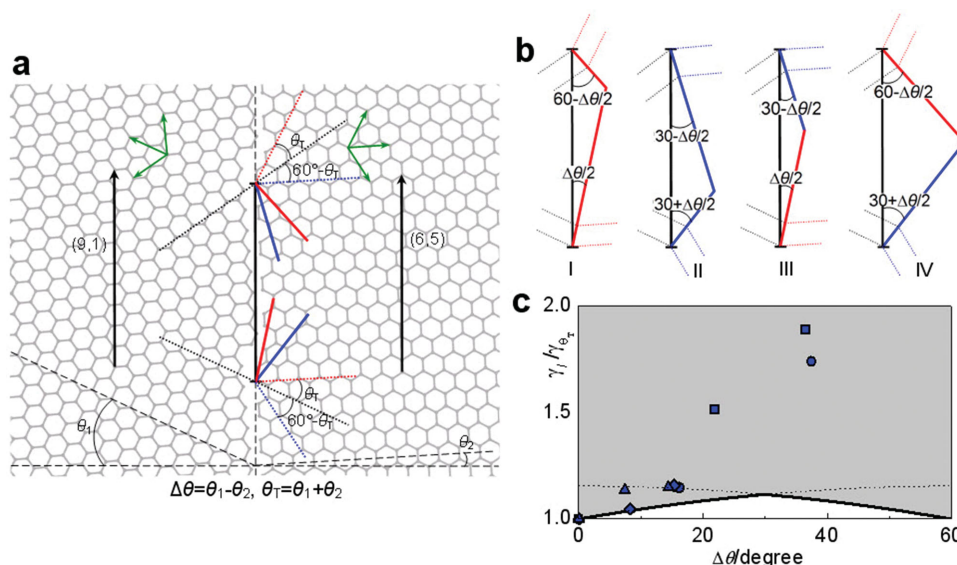
Materials
Views
www.MaterialsViews.com

Figure 1. Illustrative construction of a sinuous grain boundary in graphene. a) Framework for a GB stitching two graphene domains rotated by $\theta_1 = 25°$ and $\theta_2 = 3°$ with respect to the normal of the GB. The periodicity of the two domains are described by repeated vectors (9,1) and (6,5), respectively. The supposed linear GB (black solid line) can be folded into two bisector segments, each of which has two options shown by red and blue solid lines. The green lines denote the crystallographic orientations of the domains. b) Schematic GB units I–IV resulting from combinatorics of the bisector segments. The slant angles of bisector segments with respect to the black global line are provided. c) $\gamma_{II}/\gamma_{\theta_T}$ as functions of $\Delta\theta$ according to Equations (3) and 4 (dashed lines). The shaded region bounded by the solid line is where either Equations 3 or 4 is satisfied.

2. Results and Discussion

2.1. Phenomenological Analysis

In graphene, a GB acts as an one-dimensional interface stitching two domains that are misoriented with each other (**Figure 1**a), with a tilt angle defined as $\theta_T = \theta_1 + \theta_2$, where θ_1 and θ_2 are the angles between the crystallographic orientations of the two domains and the in-plane normal of the global GB line, respectively. The GB with $\theta_1 = \theta_2$ belongs to the symmetric or bisector type, while the GB with $\theta_1 \neq \theta_2$ belongs to asymmetric or non-bisector type. Following the Read–Shockley model, we approximately model the GB as a periodic array of dislocations. The periodicities of the domains are defined by their respective matching vectors (n_1, m_1) and (n_2, m_2), and the corresponding GB is denoted as $(n_1, m_1)|(n_2, m_2)$. According to the theory of coincidence site lattice (CSL),[39] n and m should be prime numbers, by which the GB periodicity is minimized and the coincidence sites are maximized at a given misorientation of domains. The lengths of the two matching vectors should be equal to satisfy the commensurability condition, that is, $a_0\sqrt{n_1^2 + n_1 m_1 + m_1^2} = a_0\sqrt{n_2^2 + n_2 m_2 + m_2^2}$, where a_0 is the lattice constant of graphene. Solving this equation yields either $n_1 = n_2$ and $m_1 = m_2$ or $n_1 \neq n_2$ and $m_1 \neq m_2$; the former is for the bisector GBs while the latter for the nonbisector GBs. Compared to the bisector GBs, the nonbisector GBs are much more abundant in CVD graphene samples and will be the focus of this work.

Our idea is motivated by the classical dislocation theory in solids,[40] which shows that identical edge dislocations (or clusters) energetically favor an alignment. As such, the dislocation cores (or clusters) can have their stress fields maximally cancelled out, as supported by the continuum theory based on a disclination dipole model. Therefore, the bisector GBs favor

a globally linear shape regardless of the tilt angle. Nevertheless, it is impossible for a nonbisector GB to perfectly align all the dislocations; instead, all the dislocations are slanted relative to the global GB line and one of them is distinctly misoriented owing to the broken lattice coherence across the grain boundary (Figure S1,2a,3a, Supporting Information). Forcing the randomly oriented dislocations into a roughly linear line results in high strain energy and makes the GB unfavorable. Here, we propose a way to relieve the residual stress by locally aligning the dislocations into bisector segments. As such, a repeat unit of a nonbisector GB can be folded into two bisector segments, instead of previously used linear models.[20–22] Following this idea, we start at the two ends of the repeat unit of an arbitrary nonbisector GB shown by thick black line in Figure 1a and locally construct bisector segments between the two domains. Due to the six-fold lattice symmetry, we can find three crystallographic orientations (green lines with arrow) in each domain, with a misoriented angle of θ_T between the two domains. At the lower end of the repeat unit, taking one crystallographic orientation in the left domains (black dotted line), we can principally find three crystallographic orientations in the right domains to build up a bisector segment, but only two of them (red and blue dotted lines) are usable, because the tilt angle of a grain boundary should be less than 60°. Bisecting the angle between the black and blue dotted lines determines one possible direction of a bisector segment as shown by thick blue solid line. Alternatively, bisecting the angle between the black and red dotted lines gives the direction of another bisector segment, shown by thick red solid line. Similarly, we can determine the directions of two bisector segments starting at the upper end of the repeat unit (upper blue and red solid lines in Figure 1a). The two sets of bisector segments can joint as they extend toward each other and thereby result in

www.MaterialsViews.com

ADVANCED
FUNCTIONAL
MATERIALS
www.afm-journal.de

FULL PAPER

four chevron-shaped units I–IV for the GB, as shown in Figure 1b. The two segments of the unit I are both tilted at θ_T, and slanted by $60° - \Delta\theta/2$ and $\Delta\theta/2$ ($\Delta\theta = \theta_1 - \theta_2$, $0 < \Delta\theta < 60$) with respect to the global GB line, respectively; whereas the two of the unit II are tilted at $60° - \theta_T$, and slanted by $30° + \Delta\theta/2$ and $30° - \Delta\theta/2$, respectively. The units III and IV result from the cross-combination of the bisector segments in the units I and II. These units serve as building blocks to make up s-GBs by repeating along the direction parallel to the matching vectors. Note that we neglect the bisector segments with slant angle exceeding 60° as the over-slanted segments are unlikely to result in energetically favorable s-GBs. Then, the same process applied to other crystallographic orientations does not produce new GB shape. It is interesting that the GB-I and II become bisector GBs at $\Delta\theta = 0°$ and 60°, respectively.

To verify our assumption, we first analytically compare the energy of the l- and s-GBs. For the linear grain boundaries (l-GBs), there is a common feature in their unit structures that one dislocation is distinctly misoriented and all other dislocations are slanted by $\Delta\theta/2$ from the GB line (see **Figures 2**a, **3**a and 3b). Thus the energy of a l-GB can be expressed as

$$\gamma_{l\text{-GB}} = L\gamma_l + \gamma_{kink} \tag{1}$$

where γ_l is the energy per unit length of the GB tilted at θ_T but having dislocations all slanted by $\Delta\theta/2$ from the GB line (Figure S2, Supporting Information), γ_{kink} is the energy of two kinks formed between the distinctly misoriented dislocation and its neighbors and L is length of the repeat unit. At the same tilt, the GB-I has two bisector segments tilted at θ_T and its energy can be written as

$$\gamma_{GB-I} = \gamma_{\theta_T}(L_1 + L_2) + \gamma'_{kink} \tag{2}$$

where γ_{θ_T} is the energy per unit length of the bisector GB tilted at θ_T, L_1, and L_2 are the lengths of the two segments, respectively, and γ_{kink} is the energy of two kinks formed between the segments. Our calculations tested that both γ'_{kink} and γ_{kink} are negligible compared to other terms in the equations. Thus, $\gamma_{GB-I} < \gamma_{l\text{-GB}}$ goes to $\gamma_{\theta_T}(L_1 + L_2) < L\gamma_l$. By applying an elementary law of sines to the triangle of GB-I in Figure 1b, we have $L_1 = L\sin(\Delta\theta/2)/\sin(2\pi/3)$ and $L_2 = L\sin(\pi/3 - \Delta\theta/2)/\sin(2\pi/3)$. Then, the condition for achieving $\gamma_{GB-I} < \gamma_{l-GB}$ becomes,

$$\frac{\gamma_l}{\gamma_{\theta_T}} > \frac{2\sqrt{3}}{3}\sin(\pi/3 + \Delta\theta/2) \tag{3}$$
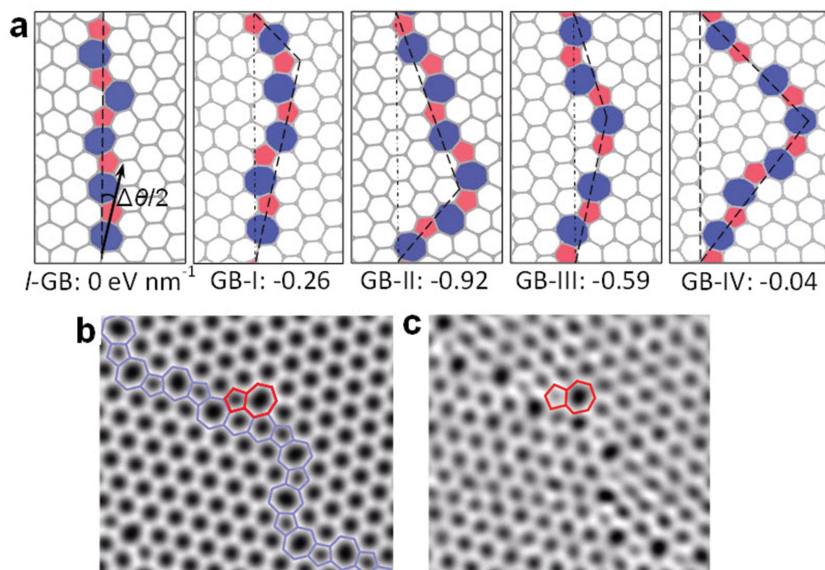

Figure 2. Preferred structure of asymmetric GBs. a) Atomic structures of linear GB (l-GB) and sinuous GB-I, II, III, IV for the (6,5)|(9,1), with $\theta_T = 28°$, $\Delta\theta = 22°$. Energy of each s-GB relative to the l-GB is listed below each figure. b) Simulated scan tunneling microscopy image of the most favorable GB-II, with a dislocation highlighted in red glided by one step. c) Experimental ADF-STEM image[9] verifies the structure in b (. Reproduced with permission. Copyright 2011, Nature.

Similar analysis applied to the GB-II results in another condition,

$$\frac{\gamma_l}{\gamma_{60°-\theta_T}} > \frac{2\sqrt{3}}{3}\cos(\Delta\theta/2) \tag{4}$$

Here, we do not account the GB-III and IV as they are unlikely to be more stable than the GB-I and II. Clearly, the s-GB is energetically more favorable than the l-GB as long as
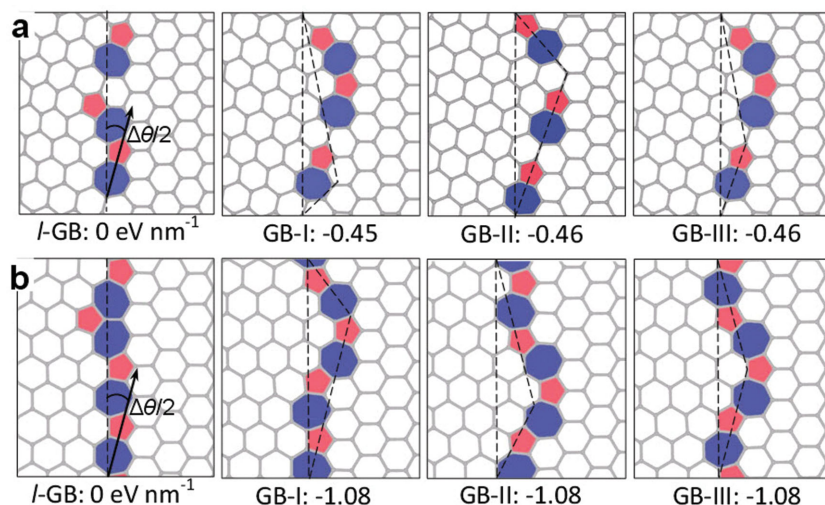

Figure 3. Favorable structure of nonbisector GBs. a) Atomic structures of (left: l-GB) linear and (right: s-GB) sinuous-shaped (5,3)|(7,0), with $\theta_T = 38°$ and $\Delta\theta = 22°$. b) Similar to (a) but for the (4,4)|(7,0), with $\theta_T = 30°$, $\Delta\theta = 30°$. The energy of the s-GB relative to the l-GB is listed below each figure. The tilt angles of the bisector segments in each GB are also provided.

**ADVANCED
FUNCTIONAL
MATERIALS**

www.afm-journal.de

*Materials
Views*

www.MaterialsViews.com

Equation 3 or 4 is satisfied. To illustrate this condition, we plot diagrams of $\gamma_l/\gamma_{\theta_T}$ and $\gamma_l/\gamma_{60°-\theta_T}$ with respect to $\Delta\theta$ in Figure 1c, where the shaded region is defined by the union set of Equations 3 and 4. As the GB raises the energy of graphene, $\gamma_l/\gamma_{\theta_T}$ must be >0 and, in most case, > 1 since γ_{θ_T} (for bisector GBs) is usually lower than γ_l (for nonbisector GBs) at the same tilt. Thus the shaded region is dominant in the diagram and dictates the GB-I as the preferred structure. If $60° - \theta_T$ is close to 32° or 22°, at which $\gamma_{60°-\theta_T}$ is particularly low,[30] Equation 4 will be easily satisfied and the GB-II lies at the ground state. However, deriving a direct relationship between $\gamma_{ll}/\gamma_{\theta_T}$ and $\Delta\theta$ is mathematically difficult, impeding a strict proof of Equations 3 and 4. Yet numerical computations allows us to roughly test these equations. Finite-long bisector GBs with tilt angles of 9°, 22°, 32° and 48° were selected for calculating γ_{θ_T}, and the dislocations are then realigned via glide to form a GB line slanted by $\Delta\theta$ from the bisecting line for calculating γ_l (see Figure S2, Supporting Information). We find that the calculated $\gamma_l/\gamma_{\theta_T}$ for all the structures fall into the shaded region regardless of $\Delta\theta$, as shown in Figure 1c, well corroborating our theory.

2.2. Atomistic Calculations and Discussions

The above analysis allows us to address the atomic structures and compare the energy of nonbisector GBs computationally. We first take (6,5)|(9,1) as a model system, with $\Delta\theta = 22°$ and $\theta_T = 28°$. According to our analysis, four s-GBs, denoted as GB-I, GB-II, and GB-III and GB-IV, can be constructed for the (6,5)|(9,1) by using the established units I, II and III, respectively, as shown in Figure 2a, together with the l-GB model.[19] All the four s-GBs are found to be more stable than the l-GB. The most stable one is the GB-II, which is 0.92 eV nm^{-1} lower in energy than the l-GB. The unit of GB-II is composed of two 32° (i.e., 60° − θ_T) bisector segments and slanted from the global GB line by 41° (i.e., 30° + $\Delta\theta/2$) and 19° (i.e., 30° + $\Delta\theta/2$), respectively. Compared with other s-GBs, the segments in the GB-II show better organzied dislocations with the maximum density, making the stress more effectively relieved. The higher stability of the GB-II agrees with our above analysis that the bisector segments tilted at 32° have a particularly low formation energy.[31] Surprisingly, the GB-II is even more stable by 0.38 eV nm^{-1} than the full bisector GB with the same tilt angle of $\theta_T = 28°$, suggesting that the sinous GBs may lie at the golobal minimum at some special grain misorientations. Energetic preference of the sinous GB should have relevance to the GB morphologies observed in experiments, leading us to examine what contrast the s-GB can generate in scan tunneling microscopy. Figure 2b shows the simulated tunneling electron microscopy (TEM) image of the GB-II, which excellently resembles an atomic-resolution scanning TEM image (see Figure 2c) of a graphene GB taken by Huang and co-workers.[8] The only difference is that the experimental image has a dislocation (highlighted in red) glided by one step, probably induced by electron beam irradiation from TEM, as also discussed by Huang et al.

We then extend our discussion to the (5,3)|(7,0) and (4,4)|(7,0) GBs, with $\theta_T = 38°$ and 30° as well as $\Delta\theta = 22°$ and 30°, respectively. For the (5,3)|(7,0), the GB-I, II and III have the same atomic structure within the periodic boundary condition and serve as the ground state (Figure 3a), which is 0.46 eV nm^{-1} more stable than the corresponding l-GB model.[21] The units of GB-I and GB-II have the segments tilted at 38° and 22°, respectively, while that of GB-III comprises a 38° segment and a 22° segment. Thus these structures will be distinguishable if the segment lengths are doubled during structural evolution by, for example, annealing. The same behavior holds for the (4,4)|(7,0), whose GB-I, II and III lie at the ground state and are up to 1.08 eV nm^{-1} more stable than its l-GB model (Figure 3b). Interestingly, the ground state structure of the (4,4)|(7,0) is exactly the same as that predicted by Li and co-workers using a global optimization search algorithm,[41] which reflects that the present analysis is not only much simpler but also rather effective to reach the ground state of a GB at a given grain misorientation.

All the GBs presented above have relatively large $\Delta\theta$. Now, we turn to examine the (6,4)|(7,3) with a small $\Delta\theta = 6°$ (and $\theta_T = 20°$). With such small $\Delta\theta$, one bisector segment in the GB-I almost follows the global GB line while the other segment is too short to hold any dislocation (**Figure 4**). As a result, the whole GB manifests as a faceted shape with misaligned bisector segments. And so does the l-GB. In contrast, the GB-II has two bisector segments tilted at 40° and appears to be more sinuous upon repetition. The GB-I is shown to be ground state as it is more stable than the GB-II by 0.54 eV nm^{-1}. The distinct ground state of a GB with a small $\Delta\theta$ can be understood by the coincident site lattice theory, which reveals that the GB should maximally adopt the optimal GB structure (i.e., bisector) and kinks must be embedded to accommodate the small deviation angle from the bisecting line (Figure 4). The kinked structure is in excellent agreement with our recent results for GBs in hybrid 2D materials, in which the GBs tend to be asymmetric to lift the lattice mismatch and shows the same faceted structures owing to small $\Delta\theta$.[42] It is quite encouraging that a recent experiment indeed observed such faceted GBs, formed via thermal annealing of CVD graphene samples.[43]

Overall, either the GB-I or II can be the ground state of a nonbisector GB depending on its tilt angle. At small $\Delta\theta$ the GB-I serves as the ground state while the GB-II can be more stable when $60° - \theta_T$ is close to 32° or 22°. Decomposing any nonbisector GBs into bisector segments should follow this criteria, and then our derived formula can be used to establish the detailed parameters for the preferred sinuous structure. However, a
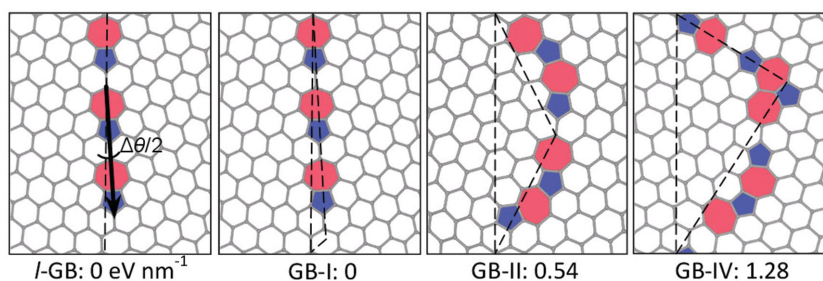

Figure 4. Atomic structures of (left: *l*-GB) linear and (right: *s*-GB) sinuous-shaped (6,4)|(7,3), with $\theta_T = 20°$ and $\Delta\theta = 6°$.

l-GB: 0 eV nm^{-1} GB-I: 0   GB-II: 0.54   GB-IV: 1.28

www.MaterialsViews.com

ADVANCED
FUNCTIONAL
MATERIALS
www.afm-journal.de

FULL PAPER

remaining question is how the analysis based on the periodically arranged bisector segments can be related to experiments, in which the GBs are mostly aperiodic.[7–12] This issue can be addressed in two aspects. First, during the course of growth, the different units can form concurrently in the same GB due to their close energies. This is evidenced in several experimental images of aperiodic GBs,[9,44–46] which can be assigned to comprise a series of bisector segments with different length and orientation (Figure S3, Supporting Information). The adopted orientation of bisector segments is particularly flexible in graphene due to the six-fold lattice symmetry, making the periodicity of s-GBs easily broken. Second, in addition to the thermodynamics, kinetic effect plays an important role in determining the GB shape, and the periodicity can be readily destroyed via dislocation migration or various defect reconstructions, which can occur as a by-product of structural characterizations with TEM (it unavoidably introduces electron beam irradiation). The eventual GB shapes also depend on the nucleation density and the detailed process of graphene growth. While further study on the aperiodic GBs is certainly needed, the scheme laid out above for building favorable s-GBs is still significant in offering a route map for experimental works in this direction.

2.3. Mechanical Strength and Electronic Transport

To complete the description of s-GBs, we further explore what properties these s-GBs can contribute in graphene. It has been predicted that the mechanical properties of graphene can be largely degraded by grain boundaries,[16,18–20] yet recent experimental measurements showed that the strength of graphene is slightly reduced despite the presence of GBs.[45,47] Using empirical molecular dynamics simulations, we show in **Figure 5**a the stress-strain curves of the most favorable s-GBs (i.e., the GB-II) subject to uniaxial strain normal to the grain boundary. Compared to the result of l-GB models, the GB strength is remarkably enhanced upon taking the sinuous shape. The enhancement is up to 27.3% for (6,5)|(9,1) s-GB and 13% for (7,0)|(5,3) s-GB. The normal strengths of the (6,5)|(9,1), (4,4)|(7,0), (5,3)|(7,0) s-GBs reach 98, 97 and 96 GPa, respectively, rivaling the strength of pristine graphene (~100 GPa) stretched in the armchair direction. The enhanced mechanical

strength of s-GBs can be understood by comparing the normal stress distributions in the l- and s-GBs of (6,5)|(9,1) and (5,3)|(7,0), as shown in Figure 5b,c. The dislocation-induced stress field is much stronger in the l-GB than that in the s-GB, echoing the latter's higher stability. Similar to the bisector GBs,[16] the highest tensile stress resides on the bonds shared by the hexagon and heptagon, which dictate the strength of most GBs. Indeed, the structural failure always starts at the bonds with the highest tension (Figure 5b,c), and the relieved bond stress in the s-GB leads to a strength close to that of perfect graphene. An exception is the (6,5)|(9,1) GB-II, in which the in-plane stress is almost eliminated; in this case, the GB failure still initiates from the bond shared by hexagon and heptagon, but no longer the one with maximum tensile stress. Instead, it is from the bond more parallel to the applied force (Figure 5b, lower), indicating that the residual stress becomes secondary to the GB strength. It is also worthwhile to note that the strength of s-GBs appears to be proportional to the tilt angle of their bisector segments, which are at 22°, 30° and 32° in the (7,0)|(5,3), (7,0)|(4,4) and (6,5)|(9,1), respectively, consistent with the trend in bisector GBs. As the experimentally measured GBs are rarely linear, the simulated mechanical properties based on s-GBs should be more relevant to reality.[45]

Another interesting property arises in electronic transport across the s-GBs. We find that the transport across all the examined s-GBs exhibits a sizeable gap, as depicted in **Figure 6** and Supporting Information Figure S4, in contrast to previous report on l-GBs which can be either transparent or reflecting depending on the matching vectors.[21,48] The transport gaps are 0.37, 0.11, 0.56 and 0.10 eV for the ground state structures of the (6,5)|(9,1), (5,3)|(7,0), (4,4)|(7,0), and (6,4)|(7,3), respectively. Note that our results for the corresponding l-GBs are in good agreement with early theory,[18] that is the (5,3)|(7,0) and (6,4)|(7,3) l-GBs are transparent while the (4,4)|(7,0) l-GB is perfectly reflective for charge carriers (see dashed lines in the right panel of Figure 6; for the (6,4)|(7,3), l-GB is the same as the GB-I). Thus, in addition to the matching vectors, the dislocation arrangement is another important factor determining the electronic transport across graphene GBs. Zhang et al. also found that the detailed dislocation arrangements can influence the transport behavior of graphene GBs.[47] Electronic structure analyses show that the sinuous shape of grain boundary either opens a band gap or causes more localized
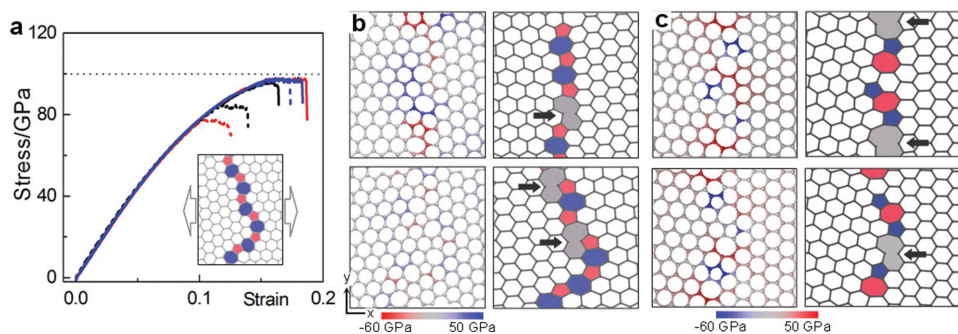

Figure 5. Mechanical properties of asymmetric GBs. a) Stress-strain curves of the (7,0)|(5,3) (black), (6,5)|(9,1) (red) and (4,4)|(7,0) (blue) GB-II subject to tension along the in-plane normal of GBs. The dashed lines show the results of the corresponding l-GBs. The insert illustrated how the GB is stretched in simulations. The dot line marks the strength of perfect graphene along armchair direction. b) Left: Maps of normal stress (σ_{xx}) in the (upper) l-GB and (lower) GB-II for the (6,5)|(9,1); right: the snapshot of the (upper) l-GB and (lower) GB-II at the initial stage of failure, with the initiated points marked by arrows. c) The same as (b) but for the (5,3)|(7,0). The stress magnitude is referenced to the color bars.
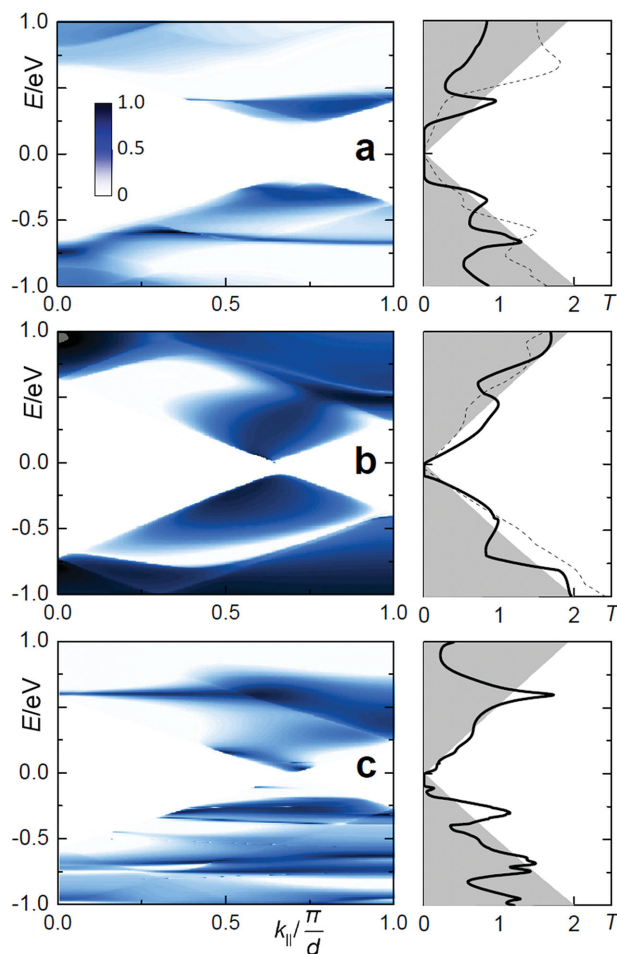
FULL PAPER

ADVANCED
FUNCTIONAL
MATERIALS

www.afm-journal.de

Materials Views

www.MaterialsViews.com

Figure 6. Electronic transport through the *s*-GBs. a) Left: Transmission probability through the ground state structure of (6,5)|(9,1) as a function of transverse momentum *k* and energy *E*; right: zero-bias total transmission per unit length through the (6,5)|(9,1) *s*-GB as a function of *E* (solid line), together with the results of the (6,5)|(9,1) *l*-GB (thin dashed line) and pristine graphene (light grey shade). b,c) The corresponding results for b) the (5,3)|(7,0) and c) the (6,4)|(7,3). The Fermi level is set to zero.

states near the Fermi level, giving rise to enhanced electronic scattering and thereby the semiconducting transport behavior. If properly engineered, the *s*-GBs may overcome the limitation of zero-gap in graphene and will be technologically promising to enable graphene devices with logic operation.

3. Conclusions

To conclude, our phenomenological analysis, combined with quantum mechanical calculations, revealed a new type of structures for asymmetric grain boundaries that are remarkably more stable than previously used models and closely resemble recent experimental observations. We show that dislocations in an asymmetric grain boundary can locally form slanted bisector segments, resulting in a well-defined sinuous shape for the whole boundary. The unusually stable sinuous structures significantly relieve the residual stress in the grain boundaries and endow them with enhanced mechanical strength. Moreover, all the sinuous grain

boundaries are found to show a sizeable gap for electronic transport, irrespective of their misorientation angles, thus opening prospect for the design of graphene-based logic devices through purposeful engineering of topological grain boundaries. Our results can also be used as a basic way for understanding the grain boundary morphologies in other two-dimensional materials, such as boron nitride and transition metal disulfides.

4. Computational Methods

The total energies of GBs are calculated using density functional theory based tight-binding (DF-TB) method with associated Slater-Koster parameters,[49] as implemented in the DFTB+ code.[50] To test the accuracy of the DF-TB method, we also calculated the energies of (5,3)|(7,0) GB structures using density functional theory (DFT) method as implemented in VASP code[51–53] and obtained qualitatively the same results. Periodic boundary conditions are adopted in all three dimensions and each supercell contains a pair of complementary GBs that are separated from each other by 30 Å. The vacuum region between images in repeated supercells is set as 30 Å to exclude any spurious interaction. The atomic positions are fully relaxed along both the in-plane and out-of-plane directions, with the supercell size adjusted correspondingly. The mechanical strength of grain boundaries (GBs) are calculated by large-scale simulations based on the Adaptive Intermolecular Reactive Empirical Bond Order (AIREBO) potential,[54] as implemented in Large-scale Atomic/ Molecular Massively Parallel Simulator (LAMMPS) code.[55] Constant atom number (N), volume (V) and energy (E) (NVE) ensemble was adopted for all the simulations, and a simulated system has an initial temperature of 0 K. The graphene sheets are simulated using supercells with a periodic boundary condition, and the neighboring periodic images are isolated by a vacuum layer of 3 nm. Uniaxial tensile strain is applied along the horizontal direction (perpendicular to the GBs) of the simulated box. The graphene sheets are stretched step by step with a strain increment of 0.05%, and, meanwhile, the dimension is allowed to shrink in the vertical direction (parallel to the GBs). The electronic transport properties of the grain boundaries were calculated using the nonequilibrium Green's function formalism, as implemented in the TRANSIESTA code.[56] The structures used for electronic transports were relaxed using DF-TB calculations. The quantum transmissions were calculated in the zero-bias regime and self-energies are included for the coupling of scattering region to the semi-infinite graphene electrodes.

Supporting Information

Schematic illustration of bisector and nonbisector GBs, analyses of experimental observed grain boundaries and transmission spectra are collected. Supporting Information is available from the Wiley Online Library or from the authors.

Acknowledgements

[1] M. Peplow, *Nature* **2013**, *503*, 327.

[2] A. K. Geim, *Science* **2009**, *324*, 1530.

[3] F. Banhart, J. Kotakoski, A. V. Krasheninnikov, *ACS Nano* **2010**, *5*, 26.

[4] M. T. Lusk, L. D. Carr, *Phys. Rev. Lett.* **2008**, *100*, 175503.

[5] Z. Xu, Y. Bando, L. Liu, W. Wang, X. Bai, D. Golberg, *ACS Nano* **2011**, *5*, 4401.

[6] J. Yin, Z. Zhang, X. Li, J. Yu, J. Zhou, Y. Chen, W. Guo, *Nat. Commun.* **2014**, *5*.

[7] K. Kim, Z. Lee, W. Regan, C. Kisielowski, M. Crommie, A. Zettl, *ACS Nano* **2011**, *5*, 2142.

[8] P. Y. Huang, C. S. Ruiz-Vargas, A. M. van der Zande, W. S. Whitney, M. P. Levendorf, J. W. Kevek, S. Garg, J. S. Alden, C. J. Hustedt, Y. Zhu, *Nature* **2011**, *469*, 389.

[9] Q. Yu, L. A. Jauregui, W. Wu, R. Colby, J. Tian, Z. Su, H. Cao, Z. Liu, D. Pandey, D. Wei, *Nat. Mater.* **2011**, *10*, 443.

[10] J. An, E. Voelkl, J. W. Suk, X. Li, C. W. Magnuson, L. Fu, P. Tiemeijer, M. Bischoff, B. Freitag, E. Popova, *ACS Nano* **2011**, *5*, 2433.

[11] D. L. Duong, G. H. Han, S. M. Lee, F. Gunes, E. S. Kim, S. T. Kim, H. Kim, Q. H. Ta, K. P. So, S. J. Yoon, *Nature* **2012**, *490*, 235.

[12] J. Coraux, A. T. N'Diaye, C. Busse, T. Michely, *Nano Lett.* **2008**, *8*, 565.

[13] P. M. Ajayan, B. I. Yakobson, *Nat. Mater.* **2011**, *10*, 415.

[14] O. V. Yazyev, Y. P. Chen, *Nat. Nanotechnol.* **2014**, *9*, 755.

[15] J. H. Warner, E. R. Margine, M. Mukai, A. W. Robertson, F. Giustino, A. I. Kirkland, *Science* **2012**, *337*, 209.

[16] Y. Wei, J. Wu, H. Yin, X. Shi, R. Yang, M. Dresselhaus, *Nat. Mater.* **2012**, *11*, 759.

[17] Y. Liu, B. I. Yakobson, *Nano Lett.* **2010**, *10*, 2178.

[18] R. Grantab, V. B. Shenoy, R. S. Ruoff, *Science* **2010**, *330*, 946.

[19] J. Zhang, J. Zhao, J. Lu, *ACS Nano* **2012**, *6*, 2704.

[20] Z. Song, V. I. Artyukhov, B. I. Yakobson, Z. Xu, *Nano Lett.* **2013**, *13*, 1829.

[21] O. V. Yazyev, S. G. Louie, *Nat. Mater.* **2010**, *9*, 806.

[22] A. W. Tsen, L. Brown, M. P. Levendorf, F. Ghahari, P. Y. Huang, R. W. Havener, C. S. Ruiz-Vargas, D. A. Muller, P. Kim, J. Park, *Science* **2012**, *336*, 1143.

[23] J. C. Koepke, J. D. Wood, D. Estrada, Z.-Y. Ong, K. T. He, E. Pop, J. W. Lyding, *ACS Nano* **2013**, *7*, 75.

[24] L. Tapasztó, P. Nemes-Incze, G. Dobrik, K. J. Yoo, C. Hwang, L. P. Biró, *Appl. Phys. Lett.* **2012**, *100*, 053114.

[25] X. Li, X. Wu, X. C. Zeng, J. Yang, *ACS Nano* **2012**, *6*, 4104.

[26] L. Kou, C. Tang, W. Guo, C. Chen, *ACS Nano* **2011**, *5*, 1012.

[27] S. S. Roy, M. S. Arnold, *Adv. Funct. Mater.* **2013**, *23*, 3638.

[28] A. W. Cummings, D. L. Duong, V. L. Nguyen, D. Van Tuan, J. Kotakoski, J. E. Barrios Vargas, Y. H. Lee, S. Roche, *Adv. Mater.* **2014**, *26*, 5079.

[29] Z. Fei, A. Rodin, W. Gannett, S. Dai, W. Regan, M. Wagner, M. Liu, A. McLeod, G. Dominguez, M. Thiemens, *Nat. Nanotechnol.* **2013**, *8*, 821.

[30] B. Yakobson, *Appl. Phys. Lett.* **1998**, *72*, 918.

[31] O. V. Yazyev, S. G. Louie, *Phys. Rev. B* **2010**, *81*, 195420.

[32] E. Cockayne, G. M. Rutter, N. P. Guisinger, J. N. Crain, P. N. First, J. A. Stroscio, *Phys. Rev. B* **2011**, *83*, 195425.

[33] P. Simonis, C. Goffaux, P. Thiry, L. Biro, P. Lambin, V. Meunier, *Surf. Sci.* **2002**, *511*, 319.

[34] W.-T. Pong, J. Bendall, C. Durkan, *Surf. Sci.* **2007**, *601*, 498.

[35] J. Červenka, C. Flipse, *Phys. Rev. B* **2009**, *79*, 195429.

[36] E. S. Penev, V. I. Artyukhov, F. Ding, B. I. Yakobson, *Adv. Mater.* **2012**, *24*, 4956.

[37] J. Zhang, J. Zhao, *Carbon* **2013**, *55*, 151.

[38] Y. Lu, J. Guo, *Appl. Phys. Lett.* **2012**, *101*, 043112.

[39] S. Ranganathan, *Acta Cryst.* **1966**, *21*, 197.

[40] J. P. Hirth, J. Lothe, *Theory of dislocations*, Wiley, New York, USA **1982**.

[41] Z.-L. Li, Z.-M. Li, H.-Y. Cao, J.-H. Yang, Q. Shu, Y.-Y. Zhang, H. Xiang, X. Gong, *Nanoscale* **2014**, *6*, 4309.

[42] Z. Zhang, Y. Yang, B. I. Yakobson, *J. Mech. Phys. Sol.* **2014**, *70*, 62.

[43] B. Yang, H. Xu, J. Lu, K. P. Loh, *J. Am. Chem. Soc.* **2014**, *136*, 12041.

[44] C. Ma, H. Sun, Y. Zhao, B. Li, Q. Li, A. Zhao, X. Wang, Y. Luo, J. Yang, B. Wang, *Phys. Rev. Lett.* **2014**, *112*, 226802.

[45] H. I. Rasool, C. Ophus, W. S. Klug, A. Zettl, J. K. Gimzewski, *Nat. Commun.* **2013**, *4*, 2811.

[46] Y. Wu, Y. Hao, H. Y. Jeong, Z. Lee, S. Chen, W. Jiang, Q. Wu, R. D. Piner, J. Kang, R. S. Ruoff, *Adv. Mater.* **2013**, *25*, 6744.

[47] G.-H. Lee, R. C. Cooper, S. J. An, S. Lee, A. van der Zande, N. Petrone, A. G. Hammerberg, C. Lee, B. Crawford, W. Oliver, *Science* **2013**, *340*, 1073.

[48] J. Zhang, J. Gao, L. Liu, J. Zhao, *J. Appl. Phys.* **2012**, *112*, 053713.

[49] C. Köhler, T. Frauenheim, *Surf. Sci.* **2006**, *600*, 453.

[50] B. Aradi, B. Hourahine, T. Frauenheim, *J. Phys. Chem. A* **2007**, *111*, 5678.

[51] G. Kresse, J. Hafner, *Phys. Rev. B* **1994**, *49*, 14251.

[52] G. Kresse, J. Furthmüller, *Phys. Rev. B* **1996**, *54*, 11169.

[53] J. P. Perdew, K. Burke, M. Ernzerhof, *Phys. Rev. Lett.* **1996**, *77*, 3865.

[54] S. J. Stuart, A. B. Tutein, J. A. Harrison, *J. Chem. Phys.* **2000**, *112*, 6472.

[55] S. Plimpton, *J. Comput. Phys.* **1995**, *117*, 1.

[56] N. Troullier, J. L. Martins, *Phys. Rev. B* **1991**, *43*, 1993.